A State Estimation Method for Estimating Electric Fields During Geomagnetic Disturbances (GMDs)

Nicole LoGiudice, *Student Member, IEEE*, Jonathan M. Snodgrass, *Senior Member, IEEE*,
Thomas J. Overbye, *Life Fellow, IEEE*
Department of Electrical and Computer Engineering
Texas A&M University
College Station, TX, USA
nicolelogiudice30@tamu.edu; snodgrass@tamu.edu; overbye@tamu.edu

***Abstract*—This work presents a state estimation method for estimating regional electric fields during geomagnetic disturbances using GIC and magnetometer measurements. The electric field is divided into spatial regions, and a weighted least squares approach is used to solve for the field components. The estimator supports a wide range of linear field structures, sensor configurations, and region definitions. Estimation performance is evaluated using a statistical cost function compared against a chi-squared threshold to assess model data consistency. Two systems are tested: a 6-bus conceptual network used to assess sensitivity to field structure and measurement density, and a 2000-bus synthetic Texas system used to examine large-scale behavior under smoothly varying fields. Results demonstrate that the estimator can produce coherent electric field estimates even under sparse measurement conditions, while also identifying structural mismatch when present. These findings support the estimator's use as a real-time electric field reconstruction tool, with built-in diagnostics for evaluating spatial assumptions.**

***Index Terms*—Geomagnetic disturbances (GMD); Geomagnetically induced current (GICs); State Estimation (SE) ; Electric Field**

I. Introduction

Geomagnetic disturbances (GMDs), driven by solar coronal mass ejections and high speed solar wind streams, interact with the Earth's magnetosphere and induce low frequency currents in the ground. These disturbances generate time varying magnetic fields, which couple into grounded infrastructure and induce quasi DC currents, known as geomagnetically induced currents (GICs), in power transmission systems [1], [2].

Once GICs enter the transmission grid, they can disrupt normal operation by causing half cycle saturation of transformers. This saturation increases the magnetizing current, resulting in elevated reactive power demand, voltage drops, and in severe cases, voltage instability leading to blackout [3]–[5]. Additionally, nonlinear transformer core behavior under half cycle saturation produces harmonic currents that can cause heating, misoperation of protective relays, and interference with sensitive equipment [6]

The March 1989 Hydro-Quebec blackout, caused by GIC induced transformer saturation and relay misoperation, left six million people without power and remains a benchmark event for understanding GMD impacts [2], [7]. Since then, studies have focused on modeling GICs using electric fields calculated from magnetometer data, system topology, and grounding characteristics [3], [8], [9].

Assessment of a GMD event requires information about the geoelectric field driving the disturbance or the resulting GIC response of the power system. Transformer neutral GICs have been measured directly through dedicated monitoring networks and DC current transducers, including the SUNBURST network and long term monitoring installations in New Zealand and North America [10]–[12]. Methods have also been developed to infer transformer GIC or GIC related quantities from reactive power absorption and wide area measurements, including measurements obtained from phasor measurement units (PMUs) [13], [14]. Similarly, electric field observations may be measured directly or calculated from ground magnetometer data using conductivity models [15]–[18]. However, these data points are all local and do not cover an entire grid for overall visibility.

This work introduces a state estimation algorithm for determining the regional electric field that drives GICs during GMDs. Rather than assuming a fixed electric field structure, the estimator uses available GIC and magnetometer measurements to solve for the spatial electric field using a weighted least squares (WLS) approach. The estimated field is then evaluated for consistency with the measurements by comparing the cost function to a chi-squared threshold.

The primary purpose of this method is to enable electric field estimation at a single time point during actual GMD events, providing a flexible and scalable tool that can operate under varying sensor deployments. In addition to supporting real time electric field estimation using grid measurements, the estimator can also be used to evaluate the validity of assumed electric field structures when desired.

While prior work such as [19] integrates GIC flow modeling with conventional AC power system state estimation, this paper focuses specifically on linear estimation and evaluation

IEEE Transactions on Power Systems 2026. ©2026 IEEE. Personal use of this material is permitted. Permission from IEEE must be obtained for all other uses, in any current or future media, including reprinting/republishing this material for advertising or promotional purposes, creating new collective works, for resale or redistribution to servers or lists, or reuse of any copyrighted component of this work in other works.

of the electric field itself. Despite the similarity in title, the objective and methodology presented here are fundamentally different and serve a distinct purpose.

[20] also estimated eastward and northward geoelectric field components, however from high-sampling-rate instantaneous voltage and current measurements at transmission line terminals. The method embeds the electric field within a detailed frequency dependent transmission line model and uses time domain equations involving consecutive time steps to estimate a spatially uniform field. In contrast, the proposed algorithm developed here uses the quasi DC network relationship between the geoelectric field and transformer neutral GICs to formulate a linear estimation problem. Each estimation time is processed independently and does not require high rate line terminal waveform measurements or information from a preceding time step.

This method supports different spatial discretizations, measurement densities, sensor types, and dependencies. The number of regions, the inclusion of magnetometer data, the placement and density of GIC sensors, and dependencies of the electric field to the measurements can all be adjusted to explore trade-offs between resolution, observability, and model accuracy. The estimator accommodates linear electric field representations and is scalable to large systems, even under limited instrumentation.

Its flexibility makes it particularly suitable for modern grid monitoring needs. Recent events, such as the May 2024 geomagnetic storm [21], together with the growing regulatory emphasis on system monitoring (NERC TPL-007-4 and FERC Order No. 830 [22], [23]), demonstrate the need for tools that evaluate the credibility of electric field models. The proposed estimator meets the demand by supporting real time electric field reconstruction and offering statistical diagnostics that inform both operations and planning.

The remainder of this paper is organized as follows. Section II provides background information. Section III describes the estimation methodology. Section IV outlines the test scenarios. Section V presents results and analysis. Section VI concludes the paper and identifies future research directions.

II. Background

A. State Estimation in Power Systems

State estimation is a core analytical technique used to infer internal system variables based on available and potentially sparse measurements. In conventional applications, it is used to estimate voltage magnitudes and phase angles from power flow and bus voltage measurements, providing a noise robust representation of grid operating conditions. The estimation is typically formulated as a Weighted Least Squares (WLS) optimization problem in which the weighted difference between the measured and modeled quantities is minimized [24], [25].

For a linear estimation problem, the measurement model is

$$\mathbf{z} = \mathbf{M}\mathbf{x} + \boldsymbol{\epsilon},\ \mathrm{Cov}(\boldsymbol{\epsilon}) = \mathbf{R}. \tag{1}$$

Here, x is the unknown state vector, z is the measurement vector, M is the measurement sensitivity matrix, ϵ is the measurement error vector, and R is the measurement error covariance matrix. The WLS estimate minimizes

$$J(\mathbf{x}) = (\mathbf{z} - \mathbf{M}\mathbf{x})^{\mathsf{T}}\, \mathbf{R}^{-1}\, (\mathbf{z} - \mathbf{M}\mathbf{x})\,. \tag{2}$$

Measurements with smaller assigned variances receive greater weight in the estimation. The system is observable when the measurement sensitivity matrix contains independent information about every state:

$$rank(\mathbf{M}) = n_x \tag{3}$$

where n_x is the number of estimated states. Having at least n_x measurements is necessary but is not sufficient if the measurement sensitivities are linearly dependent.

In the context of geomagnetic disturbances, the estimation objective shifts from traditional AC states to the regional electric field. The electric field is a continuous physical quantity spread across a geographic area. To obtain a finite dimensional state, the system footprint can be divided into spatial regions, with each region represented by eastward and northward components. This spatial discretization representation is conceptually similar to techniques used in atmospheric science, such as the NCEP/NCAR Reanalysis Project, where spatially distributed variables are estimated using sparse observations and physical models [26].

B. Electric Field Measurements

Monitoring geomagnetic disturbances requires observations of the driving geophysical conditions and the resulting response of the power system. Magnetometers measure temporal variations in the Earth's magnetic field. These magnetic field observations, together with a model of the Earth's conductivity structure, can be used to calculate the surface electric field that drives GICs in large scale electrical grids [27]–[29].

A common implementation involves applying the plane wave method, where the horizontal components of the electric field are related to the time derivatives of the magnetic field via Earth's surface impedance tensor [30]. This method assumes a uniform Earth conductivity structure and is more accurate for regions with relatively simple geography [31]. For areas with more complex subsurface conductivity, models are employed to better capture spatial heterogeneity, which improves electric field calculations [32].

The estimator described in this paper can incorporate direct electric field measurements when available, though such data is not required. In most applications, electric field measurements are not directly recorded, but instead derived from magnetometer observations. When included, each observation represents an eastward and northward electric field component at a known geographic location and time. Uncertainty introduced by magnetometer error, conductivity modeling, and data processing is represented through the measurement error covariance matrix.

C. GIC Modeling and Measurements

The surface electric field produces an induced voltage along each transmission line path. For a line extending from bus i to bus j, the induced voltage is

$$V_{\mathrm{ind},ij}(t) = \int_{\mathcal{L}_{ij}} \mathbf{E}(\mathbf{r}, t) \cdot d\boldsymbol{\ell}. \tag{4}$$

If the electric field is uniform along a straight line segment, Equation 4 becomes

$$V_{ind,ij}(t) = E_x(t)\Delta_{x,ij} + E_y(t)\Delta_{y,ij} \tag{5}$$

where $\Delta_{x,ij}$ and $\Delta_{y,ij}$ are the eastward and northward geographic displacements of the line segment. Consequently, the induced voltage depends on the line's length and orientation as well as the magnitude and direction of the electric field. If a line crosses multiple field regions, the contributions from its within region segments can be calculated separately and summed.

Because GMD variations are generally slow relative to the power system frequency, their interaction with a transmission network is commonly represented using a quasi-DC resistive model. Transmission lines are represented by their DC resistances, while grounded transformer windings and substation grounding resistances provide conductive paths between the network and the Earth [33], [34]. In compact form, the network equations can be written as

$$\mathbf{G}\mathbf{V} = \mathbf{I}_{\mathrm{src}}(\mathbf{E}). \tag{6}$$

where $\mathbf{G}$ is the quasi DC nodal conductive matrix, V contains the quasi DC bus voltages, and $\mathbf{I_{src}}(\mathbf{E})$ contains the equivalent current injections produced by the induced line voltages. For a fixed network topology and a linear representation of the electric field, the equivalent current source vector $\mathbf{I_{src(E)}}$ is a linear function of the electric field state vector $\mathbf{E}$.

The resulting linear relationship between the electric field and transformer neutral GICs has been evaluated using both simulated systems and utility measurements [35]. The results indicated the errors arise primarily from uncertainty in the network parameters and electric field representation, particularly substation grounding resistances and spatial variations in the field, rather than from the linear form of the quasi DC network equations.

Transmission line resistance, line geography, network topology, transformer winding configuration, and grounding resistance determine how the induced current is distributed through the network. In particular, substation grounding resistance can significantly affect the magnitude and distribution of transformer neutral GICs [36].

GICs measured at grounded transformer neutrals provide direct observations of the power system's electrical response to the external field [2], [37]. A set of signed transformer neutral GIC measurements can be represented generally as

$$\mathbf{Z}_{\mathrm{GIC}} = \boldsymbol{\Phi}_n \mathbf{V} + \boldsymbol{\epsilon}_{\mathrm{GIC}}. \tag{7}$$

where $\boldsymbol{\Phi}_n$ maps the quasi DC bus voltages to the monitored transformer neutral currents and ϵ_{GIC} represents measurement error. Neutral current monitoring is operationally relevant because GIC is associated with transformer half cycle saturation and documented system impacts during geomagnetic storms [6], [38]–[41]. For the estimator, however, its central value is that it supplies a measurable output of the quasi DC network. Combining Equation 6 and Equation 7 provides the forward relationship between the electric field and the measured transformer neutral GICs. This relationship can then be incorporated into the state estimator to determine the electric field that best explains the observed GICs.

III. Methodology

This section develops the measurement sensitivity matrix that relates the regional electric field state to transformer neutral GIC measurements. Once this matrix is constructed, the measured GICs and optional electric field observations are combined in a WLS estimate. The formulation builds on the regional estimator introduced in [42], which estimated electric fields that were already discretized into fixed regions. This work addresses the challenge of estimating a spatially continuous electric field. In addition, this algorithm evaluates how well a chosen electric field assumption explains observed GIC and magnetometer data during GMDs.

A. Regional Electric Field State

Let $\mathbf{E} \in \mathbb{R}^k$ represent the electric field model being tested, where k is the number of parameters describing the field. The estimation method is general and supports any linear field representation.

To approximate a spatially continuous electric field, the geographic area covering the power system is divided into a set of non-overlapping regions. These regions are customizable and can be defined based on a regular grid, Voronoi cells around buses, administrative boundaries, or any other segmentation that fully covers the study area. The only requirement is that the regions partition the grid without gaps or overlaps, ensuring each transmission line segment and bus belongs to exactly one region.

In this study, the electric field is modeled as a continuous spatial quantity, approximated using regionally uniform eastward ($\mathbf{E_x}$) and northward ($\mathbf{E_y}$) components. With r total regions, the state vector is defined as:

$$\mathbf{E} = \begin{bmatrix} E_{x1} \\ E_{y1} \\ E_{x2} \\ E_{y2} \\ \vdots \\ E_{xr} \\ E_{yr} \end{bmatrix} \in \mathbb{R}^{2r} \tag{8}$$

Alternative models, such as a global uniform field, single region approximation, or rotated directional basis, can also be evaluated by adjusting the structure of $\mathbf{E}$ and the associated sensitivity matrices described below.

B. Electric Field to Network Mapping

Section II established the quasi DC network relationship (Equation 6) where $\mathbf{I_s rc(E)}$ contains the nodal current injections produced by the electric field. For a fixed network and a linear definition of $\mathbf{E}$, these injections are linear in the state. The matrix $\mathbf{H} \in \mathbb{R}^{n\times k}$ is defined such that $\mathbf{I_{src(E)}} = \mathbf{HE}$. Substituting this relationship into the quasi DC network equation gives $\mathbf{GV} = \mathbf{HE}$ or

$$\mathbf{V} = \mathbf{G^{-1}HE} \tag{9}$$

where n is the number of nodes in the quasi DC network, $\mathbf{V} \in \mathbb{R}^n$ contains the nodal voltage potentials, and $\mathbf{G} \in \mathbb{R}^{n\times n}$ is the network conductance matrix defined in Section II.

Each column of $\mathbf{H}$ represents the nodal current injections produced by one electric field state. The within region line segments described in Section II are used when a transmission line crosses a regional boundary. Repeating this process for all k states produces $\mathbf{H}$.

The matrix $\mathbf{H}$ incorporates the regional boundaries, transmission line geometry, line conductances, and the orientation of each line relative to the corresponding eastward or northward field component. It is an intermediate sensitivity matrix mapping the electric field to nodal current injections; it is not the final measurement sensitivity matrix used in the estimator.

The conductance matrix $\mathbf{G}$ is symmetric and typically positive semi-definite. When the network is not fully grounded or contains isolated components, the matrix may be singular, and the inverse is replaced by a symmetric pseudo-inverse to compute a consistent voltage solution.

C. Transformer GIC Measurement Mapping

Let l be the number of monitored transformer neutrals. As defined in Section II, $\Phi_n \in \mathbb{R}^{l\times n}$ maps the quasi DC nodal voltages to the corresponding signed transformer neutral currents. The modeled GIC vector is:

$$\mathbf{I_{GIC}} = \mathbf{\Phi_n V} = \mathbf{\Phi_n G^{-1} HE} = \mathbf{A}_{\text{GIC}}\mathbf{E} \tag{10}$$

where $\mathbf{A_{GIC}} = \mathbf{\Phi_n G^{-1} H} \in \mathbb{R}^{l\times k}$.

The matrix $A_{\mathbf{GIC}}$ is the sensitivity matrix relating the electric field state directly to the selected transformer neutral GICs. Row i describes how the current measured by GIC sensor i responds to each component of E, while column j describes how the jth electric field state affects all monitored transformers.

The measured GIC vector is represented as $\mathbf{Z_{GIC}} = \mathbf{A_{GIC}E}$. Although a GIC sensor is installed at a particular transformer, its measurement may be sensitive to electric field components in several regions because $\mathbf{A_{GIC}}$ includes the response of the interconnected quasi DC network.

D. Combined Measurement Model

When electric field observations are available, potentially from magnetometers, they are incorporated into the same measurement model. Let m be the number of magnetometer sites. Each site supplies an eastward and northward electric field observation, which are collected in $\boldsymbol{Z}_{\mathbf{E}} \in \mathbb{R}^{2m}$.

The matrix $\boldsymbol{A}_{\mathbf{E}} \in \mathbb{R}^{2m\times k}$ maps the electric field state to these observations. For the regional state in Equation 8, a row associated with an eastward observation in region q has a value of one in the column corresponding to E_{xq} and zeros elsewhere. A northward observation in that region similarly selects E_{yq}.

The electric field and GIC measurements are stacked to form the complete measurement model:

$$\begin{aligned} &\mathbf{Z} = \begin{bmatrix} \mathbf{Z_E} \\ \mathbf{Z_{GIC}} \end{bmatrix}, \quad \mathbf{A} = \begin{bmatrix} \mathbf{A_E} \\ \mathbf{A_{GIC}} \end{bmatrix} \\ &\mathbf{Z} \in \mathbb{R}^p, \quad \mathbf{A} \in \mathbb{R}^{p\times k}, \quad \text{where } p = 2m + l \\ &\mathbf{Z} = \mathbf{AE} \end{aligned} \tag{11}$$

Thus $\mathbf{A}$ is the final measurement sensitivity matrix used by the state estimator. Its upper rows directly relate $\mathbf{E}$ to the available electric field observations, while its lower rows relate $\mathbf{E}$ to the transformer neutral GIC measurements through the quasi DC network.

If no electric field measurements are available, $m = 0$ and the corresponding rows are omitted. The estimator then operates using only $\mathbf{Z_{GIC}}$ and $\mathbf{A_{GIC}}$.

Although time indices are omitted from the preceding equations for notation simplicity, each state estimate is assigned an estimation timestamp t_k and is denoted by $\hat{\mathbf{E}}(t_k)$. All measurements are assumed to be time stamped using a common time reference. For the numerical studies presented here, the measurements used to form $\mathbf{Z}(t_k)$ are assumed to correspond to the same time instance. In a practical implementation, measurements with slightly different timestamps may be aligned to the same estimation time. A measurement recorded at time t_i is included only if

$$0 \le t_k - t_i \le \Delta t_{max} \tag{12}$$

where Δt_{max} is the maximum allowable measurement age. Because the electric field may change within one minute, a short acceptance window on the order of 10 seconds would accommodate typical SCADA communication delays while excluding stale measurements. Measurements outside this window are not included in $\mathbf{Z}(t_k)$. Each estimate is still computed independently.

E. Weighted Least Squares Estimation

Let $\mathbf{R} = \text{covariance}(\epsilon) \in \mathbb{R}^{p\times p}$ denote the measurement error covariance matrix, and define the weight matrix as $\mathbf{W} = \mathbf{R^{-1}}$.

In this study, the measurement errors are treated as independent, so $\mathbf{R}$ is diagonal and each diagonal element contains the variance assigned to the corresponding measurement. The formulation can also accommodate a non-diagonal $\mathbf{R}$ when measurement error correlations are known.

Applying the WLS formulation introduced in Section II to the measurement model in Equation 11, the estimation cost is:

$$\mathbf{J}(\mathbf{E}) = (\mathbf{Z} - \mathbf{AE})^{\mathbf{T}}\mathbf{W}(\mathbf{Z} - \mathbf{AE}), \tag{13}$$

and the estimated electric field state is defined by

$$\hat{\mathbf{E}} = \arg\min_{\mathbf{E}} \mathbf{J}(\mathbf{E}). \tag{14}$$

The vector $\mathbf{Z} - \mathbf{AE}$ is the difference between the observed measurements and those predicted for a candidate electric field state. Weighting this residual by $\mathbf{W}$ causes measurements with smaller assigned variances to have greater influence on the estimate.

When $\mathbf{A}$ has full column rank, the WLS problem has the closed form solution

$$\hat{\mathbf{E}} = (\mathbf{A}^{\mathbf{T}}\mathbf{W}\mathbf{A})^{-1}\mathbf{A}^{\mathbf{T}}\mathbf{W}\mathbf{Z}. \tag{15}$$

Equation 15 is the state estimator used in this study. The measured values enter through $\mathbf{Z}$, the relationship between the electric field and the measurements is contained in $\mathbf{A}$, and the assumed measurement uncertainties are represented by $\mathbf{W}$.

A unique unregularized estimate requires

$$rank(\mathbf{A}) = k. \tag{16}$$

Having $p \geq k$ measurements is therefore necessary but not sufficient. The rows of $\mathbf{A}$ must provide independent information about all k electric field states. Measurement configurations that do not satisfy Equation 16 are unobservable and cannot produce a unique estimate using Equation 15.

For a fixed network topology, regional definition, and sensor configuration, $\mathbf{A}$ and $\mathbf{W}$ can be constructed before processing the measurements. A new $\mathbf{Z}$ is then formed and Equation 15 is solved independently at each evaluated time point. If the network topology, regional definition, sensor placement, or assumed measurement uncertainty changes, the corresponding matrices must be updated.

F. Estimation Cost Consistency Test

After calculating $\hat{\mathbf{E}}$, the minimized estimation cost is:

$$J = (\mathbf{Z} - \mathbf{A}\hat{\mathbf{E}})^{\mathbf{T}}\mathbf{W}(\mathbf{Z} - \mathbf{A}\hat{\mathbf{E}}). \tag{17}$$

If the linear measurement model is correct, $\mathbf{A}$ has full column rank, and ϵ is a zero mean Gaussian error vector with covariance $\mathbf{R}$, then J follows a chi-squared distribution with $p - k$ degrees of freedom:

$$J \sim \chi^2(p - k) \tag{18}$$

The comparison requires $p - k > 0$. An exactly determined system with $p = k$ may produce an electric field estimate, but it has no measurement redundancy with which to evaluate residual consistency.

At a significance level of 0.05, consistency between the selected electric field model and the measurements is considered inconsistent when

$$J > \chi^2(p - k, 0.95). \tag{19}$$

A value below this threshold indicates that the residual is consistent with the variation expected from the specified measurement errors. A value above this threshold indicates that the measurements cannot be reproduced within the expected measurement uncertainty.

An elevated cost does not, by itself, identify the source of inconsistency. It may result from an inadequate electric field representation, inaccurate network parameters, erroneous measurements, or an incorrectly specified covariance matrix. In the simulations presented in this paper, the network parameters and measurement error distributions are specified. The test can therefore be used to examine whether the selected regional representation adequately describes measurements generated by the applied spatially varying field. Accordingly, J is interpreted as a model measurement consistency statistic rather than a direct measurement of error relative to a unique true regional state.

G. Customizing for Alternative Assumptions

The estimation algorithm supports any linear parameterization of the electric field. While the default structure assumes regionally uniform eastward and northward components, the state vector $\mathbf{E}$ can be redefined to represent other linear models. For instance, the number of regions can be reduced to produce a uniform field approximation, a rotated directional basis can be used, or constraints can be introduced across regions to enforce continuity or shared directional structure.

These modifications involve redefining the structure of $\mathbf{E}$ and constructing a new sensitivity matrix $\mathbf{A}$. Because the formulation remains linear, the core estimation algorithm and statistical interpretation remain unchanged. This enables estimation of electric fields under custom structural assumptions, allowing the algorithm to support a wide range of modeling strategies within the same linear formulation.

H. Practical Implementation Requirements

Implementations of the proposed framework requires both measurement infrastructure and an appropriate quasi DC network model. Transformer neutral GIC and available electric field measurements must then be assembled into the measurement vector $\mathbf{Z}$.

The network model must include the transmission system topology, line dc resistances and geographic orientations, transformer winding configurations and resistances, and substation grounding resistances. The number and placement of measurement devices must be sufficient for $\mathbf{A}$ to satisfy the full column rank condition in Equation 16. Because each electric field observation provides eastward and northward components, whereas each transformer neutral GIC monitor provides one current measurement, the required number of physical devises depends on the selected combination of the two measurement types.

No specialized computational hardware is inherent to the proposed framework.

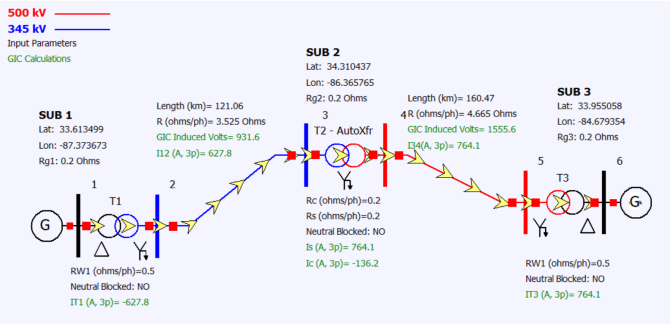

Figure 1. Conceptual 6-Bus System

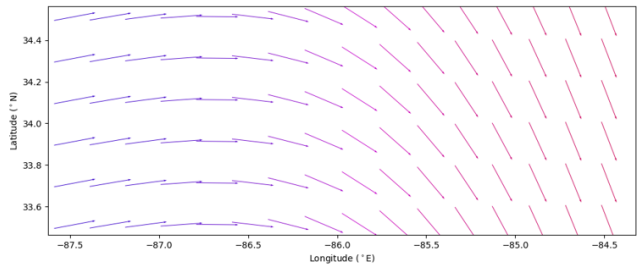

Figure 2. Conceptual 6-Bus System Constant Magnitude Electric Field with Magnitude of 5 V/km, 10 Curvature, 0.00 Angle

IV. Scenarios

To evaluate the electric field estimation framework and assess its effectiveness under varying spatial conditions and measurement densities, simulations were conducted on two networks: a conceptual 6-bus system (Figure 1) and the 2000-bus synthetic Texas system developed by Texas A&M University [43]. Both systems are subjected to synthetic electric fields constructed using a defined parameter space. The WLS cost function, evaluated against a chi-squared threshold, is used to determine the quality of the estimated electric fields.

A. Electric Field Generation

A set of spatially varying surface electric fields were applied to both systems. The fields were constructed based on the formulation introduced in [44], which models electric fields with varying magnitude, curvature, and directional orientation. The synthetic electric fields were generated using the following parameter grid:

- Field magnitudes: {1,5,7} V/km,
- Curvature values: {0,5,10} (spatial modulation)
- Rotation Angles: {0.00,0.66,1.49,2.31} radians.

These parameters produced 36 unique electric field scenarios, each representing a distinct spatially non-uniform GMD condition. The synthetic electric fields themselves are not piecewise constant across regions; instead, they vary continuously across the geographic domain. An example field generated for the 2000-bus case is shown in Figure 3.

The electric fields are grouped into four structural categories, which define how magnitude and direction vary across space:

- Constant magnitude and constant direction (0 curvature),
- Random magnitude and constant direction,
- Constant magnitude with random direction,
- Random magnitude and direction,

The constant magnitude and direction category uses a single curvature value of 0 to maintain spatial uniformity, but still applies all combinations of magnitude and rotation angle to define different uniform fields. The other three categories use the full parameter grid, with spatial variation introduced by curvature values of 5 and 10. Within the electric field generation process, the magnitude and/or direction is constrained

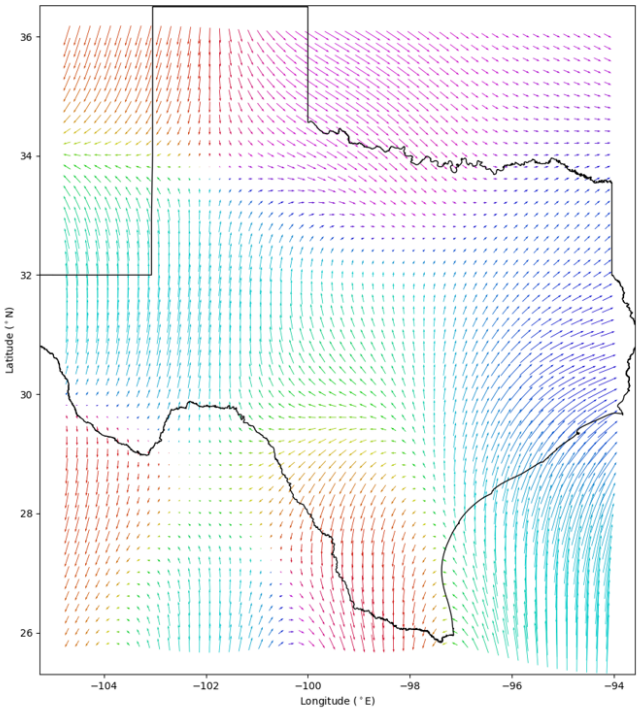

Figure 3. 2000-Bus Electric Field at 7 V/km, 10 Curvature, 0.00 Angle

according to the field category while the remaining parameters were varied to produce diverse spatial field structures. Figure 2 depicts an electric field with a constant magnitude of 5 V/km and 10 curvature.

The 6-bus system is used to evaluate all four field categories, while the 2000-bus Texas system uses only the most complex case: random magnitude and direction.

The electric field realization is generated randomly based on these parameters. This means that increasing the magnitude from 1 to 5 to 7 V/km does not simply scale a fixed field pattern. Instead, each field has a new spatial distribution. This ensures that the 36 electric field scenarios reflect a broad and diverse set of possible GMD induced field configurations, rather than scaled versions of a single shape.

The field magnitudes correspond to the maximum electric field magnitude present in the spatial grid. Using multiple magnitudes allows assessment of estimator performance under

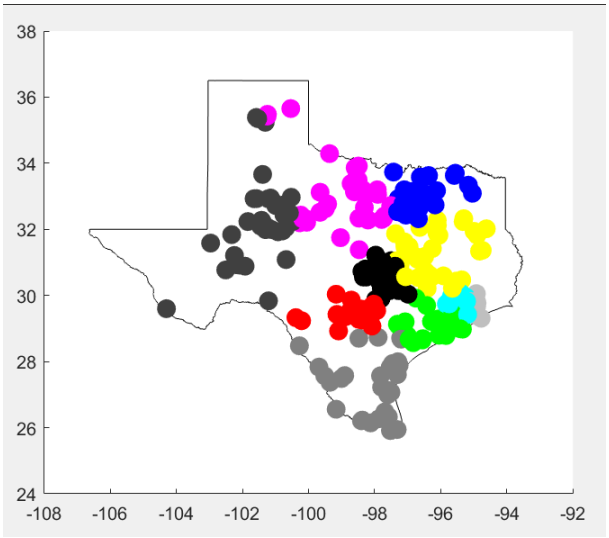

Figure 4. 2000-Bus, Transformer K-Means Constrained Clustering for 10 Clusters

both weak and extreme storm scenarios. Additionally, varying the curvature controls how spatially complex the field is, low curvature yields a nearly uniform field across the system, while high curvature introduces sharp variations between nearby points. This reflects realistic conditions where the induced electric field could vary significantly even over short distances, depending on ground conductivity and storm dynamics. The rotation parameter further diversifies the scenarios by taking the magnitude and curvature realization and rotating the electric field vector across the grid by a specified angle. This simulates directional variability and ensures the electric field is applied in a range of orientations relative to the transmission lines. Since GICs are typically strongest when the electric field is aligned parallel to a transmission line, rotating the field direction captures how estimation performance is influenced by field line orientation alignment.

B. Regional Discretization

Transformers were grouped into geographic regions based on latitude/longitude using constrained k-means clustering implemented via the KMeansConstrained Python package [45]. This method partitions transformers based on latitude and longitude while enforcing equal sized clusters, thereby preventing region imbalance. This improves upon prior work, where some regions dominated the estimation due to containing disproportionately many transformers, while others contained too few to be informative. Figure 4 shows the clusters used for 10 clusters across the respective transformers.

Once the clusters are defined, convex hulls are drawn around each group of transformers to form closed region boundaries. The centroids of these convex hulls are then used to generate a Voronoi diagram, which establishes the final spatial partitioning of the electric field estimation regions. This process creates contiguous, non-overlapping regions that reflect transformer spatial density while maintaining consistent area coverage.

C. Measurement Configuration

Two types of measurements are used in the electric field estimation framework: GIC measurements and direct electric field measurements derived from magnetometer sites, when available. These combined measurements serve as inputs to the state estimator, which solves for the regional electric field components using the weighted least squares formulation described in Section III.

Electric field observations represent regional Ex and Ey values at specific magnetometer locations. When magnetometer measurements are available, they are incorporated into the estimation process by expanding the measurement vector and the system matrix to include direct electric field observations.

In the 2000-bus system, electric field measurements are derived from a set of magnetometers placed at specific geographic locations across Texas. These locations include Amarillo, Odessa, Stephenville, Overton, RELLIS, Beaumont, and Beeville. These sites correspond to stations in the Texas A&M University Magnetometer Network (TAMUMN), which provides magnetic field data for geomagnetic disturbance monitoring in the Texas region [46], [47]. This network is used due to the limited spatial coverage of public NERC magnetometer data within Texas.

For the 6-bus system, a single magnetometer is added to the network at an arbitrarily chosen location. This location is selected once and held constant for all electric field scenarios and measurement configurations. GIC measurements are then added incrementally from zero to all three available transformer neutrals to explore how estimator performance changes with measurement count, starting from a magnetometer only configuration.

In the 2000-bus case, GIC measurements are arbitrarily selected from transformer neutrals. The number of measurements varied across configurations to evaluate estimator performance under different levels of measurement coverage. In each configuration, GIC sensors are evenly distributed across regions, meaning that each region receives the same number of measurements. While this distribution is not required for observability, the system is observable so long as A within Equation 11 is full rank. This constraint is applied to isolate the effect of increasing measurement density without introducing regional imbalance. In practice, GICs are system-wide currents and can inform regions beyond where they are physically measured.

For each electric field scenario, synthetic GIC and magnetometer measurements were calculated and observed. Measurement noise was added to both GIC and electric field data, but with different noise levels to reflect their different levels of uncertainty. Gaussian noise with a standard deviation of 0.3 A was applied to GIC measurements, while electric field observations were assigned a noise level of 0.6 V/km to reflect environmental variability and interpolation uncertainty:

$$\text{GIC Measurement Noise} \sim \mathcal{N}(0, 0.3) \tag{20}$$

$$\text{Electric Field Measurement Noise} \sim \mathcal{N}(0, 0.6) \tag{21}$$

Electric fields were modeled in volts per kilometer (V/km), and GICs in amperes (A). The conductive matrix $\mathbf{G}$ was inverted using the symmetric pseudo inverse function: $\mathbf{G^{-1}} = \text{scipy.linalg.pinvh}(\mathbf{G})$. For each electric field realization, GIC measurements, and electric field measurements when available, were used to estimate the regional electric fields.

D. Estimation Evaluation

Estimation quality is evaluated using the WLS cost function, Equation 17. The resulting cost function values J are averaged across all iterations and electric field scenarios. This average cost provides a robust indicator of estimation performance for each region and sensor configuration, smoothing out the effects of random noise and field orientation.

The average value of J is compared against the 95th percentile of a chi-squared distribution with degrees of freedom equal to the number of measurements minus the number of estimated variables. If the averaged J value falls below this threshold, the estimated electric field is considered statistically comparable to an ideal fit under Gaussian assumptions.

This approach provides a clear statistical basis for evaluating how estimator accuracy scales with sensor availability and region complexity.

V. Results

This section demonstrates the application of the proposed estimator for determining electric fields from GIC and magnetometer data during geomagnetic disturbances. The results shown here are not intended to provide universal accuracy benchmarks, as estimation performance depends on the choice of regions, sensor locations, and the true electric field structure. Instead, they highlight how the estimator behaves under different modeling choices and data configurations, and how its outputs can be interpreted in practice.

The first system is a 6-bus conceptual network used to reveal estimator behavior under tightly controlled conditions. The second is a 2000-bus synthetic model of the Texas grid used to explore performance under realistic spatial variability. In both cases, estimation cost is computed and compared to statistical thresholds to illustrate how the estimator responds to different levels of spatial structure and measurement redundancy.

A. 6-Bus Case

The 6-bus test system serves as a minimal, controlled environment to observe how the estimator responds to known electric field conditions and the number of available GIC sensors. This system contains three transformers and a single magnetometer placed at an arbitrarily chosen, fixed location. GIC measurements are incrementally added from zero to three, allowing the system to progress from an exactly determined state (with only one Ey/Ex constraint from the magnetometer) to an overdetermined one.

In this system, four electric field structures are tested:

- Constant magnitude and constant direction,
- Random magnitude and constant direction,
- Constant magnitude with random direction,
- Random magnitude and direction.

Each structure reflects a different level of spatial variability. For each case and each number of GIC sensors, the average WLS cost is computed and compared to the chi-squared 95% and 5% confidence bounds shown in Table I. These thresholds provide statistical reference points: a cost below the 95th percentile implies that the assumed model is statistically consistent with the data.

When zero GIC measurements are included, the system has zero degrees of freedom and the cost is nearly zero across all cases. This is expected. With only two measurements, Ex and Ey of the magnetometer, and no redundancy, the system is exactly solved.

As GIC measurements are added, the system gains more degrees of freedom and the cost increases. Importantly, this increase is not merely due to noise; it reflects structural mismatch between the assumed model and the true electric field. Because the estimator assumes the field is constant within each region, any spatial variation introduces differences.

This effect is most evident in the "constant direction" case, where variation in magnitude, without any flexibility in direction, produces the largest mismatch between synthetic data and the estimator's uniform field model. In contrast, the lowest costs are observed when the true electric field is uniform in both magnitude and direction, matching the estimator's assumptions exactly.

Even in small systems, this case demonstrates the estimator's ability to determine electric fields while exposing the influence of structural assumptions on fit through the use of its internal cost metric. As the true field structure becomes more complex, the estimator's limited degrees of freedom can no longer fully capture the variation, resulting in higher estimation cost. This cost behavior offers insight into when additional modeling flexibility may be warranted.

In real-time settings, where spatial field behavior is unknown and only a limited number of GIC and magnetometer sensors are available, the estimator provides a practical way to compute a best-fit field consistent with observed data.

B. 2000-Bus Case

The second case applies the estimator to a large scale synthetic Texas system with 2000 buses, 860 transformers, and 7 magnetometers. Here, the aim is to evaluate how well a piecewise constant electric field assumption holds up under realistic conditions, where the true electric field varies continuously in both magnitude and direction.

In this case, the number of regions and GIC sensors are varied to test how performance is affected. Since each region introduces two state variables (Ex and Ey), increasing the number of regions increases the dimensionality of the estimation problem. Therefore also increasing the number of measurements needed to maintain observability and accuracy.

Figure 5 shows the average values of the WLS cost function J for four different region counts, 25, 50, 75, and 95, plotted against the total number of GIC sensors used. The corresponding chi-squared thresholds are shown as dashed lines.

Table I
AVERAGE WLS COST BY NUMBER OF GIC MEASUREMENTS UNDER DIFFERENT ELECTRIC FIELD STRUCTURES

# GIC Meas.	Chi2 Upper 95%	Chi2 Lower 5%	Estimation Cost			
			Const. Mag. & Dir.	Const. Magnitude	Const. Direction	Var. Mag. & Dir.
0	0	0	1.70E-30	1.98E-30	1.14E-30	1.35E-30
1	3.841459	0.003932	0.939967	2.559437	8.033863	3.363241
2	5.991465	0.102587	2.633109	6.208690	17.21764	5.906956
3	7.814728	0.351846	1.675927	7.731462	16.61675	7.410866

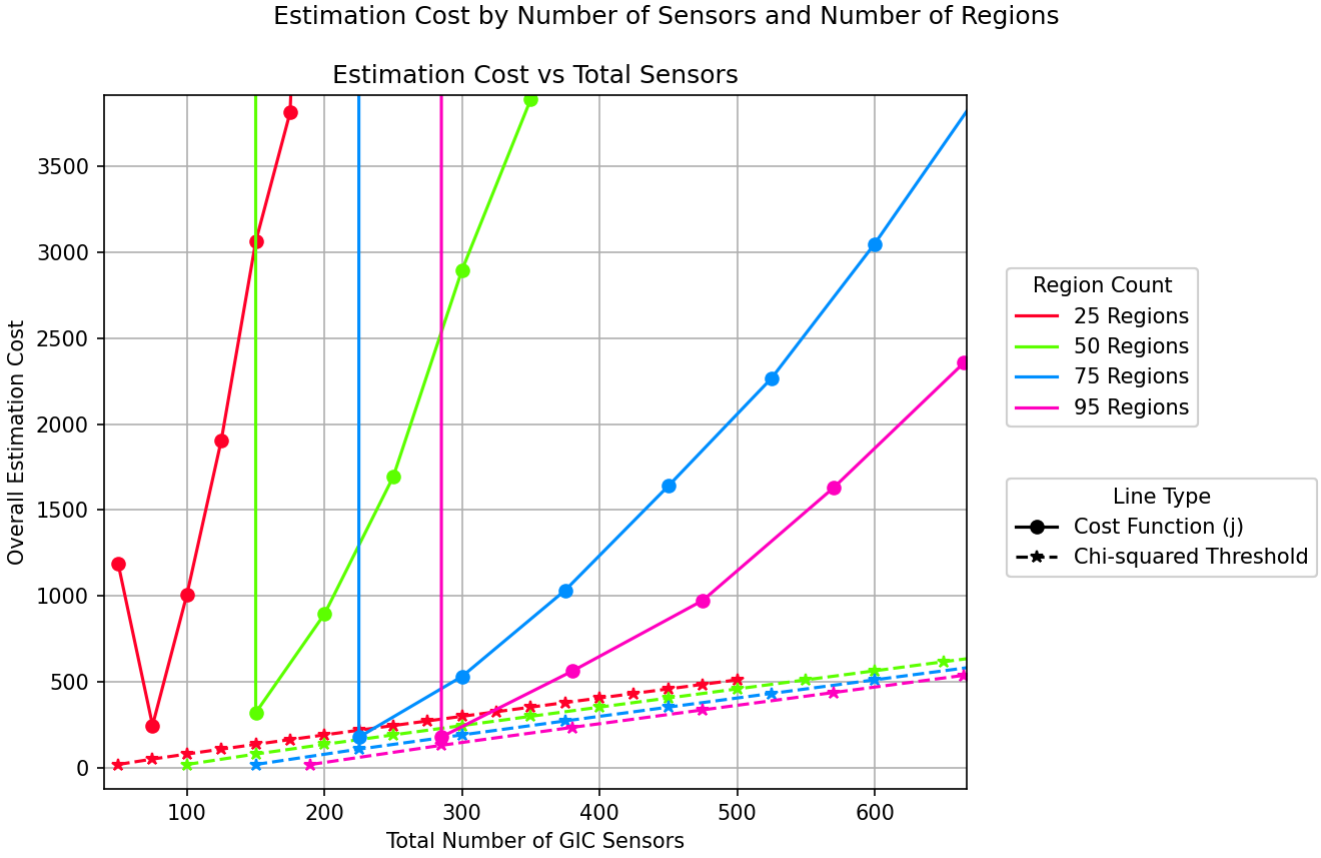

Figure 5. Average Estimation Cost for the 2000-Bus Case as a Function of GIC Sensor Count and Region Granularity, Compared to Chi-Squared 95th Percentile Threshold

For each region count, a sharp drop in cost occurs when the number of GIC sensors reaches approximately three times the number of states. This "3:1 measurement-to-state ratio" marks the point of peak estimator performance. However, beyond this point, the cost begins to rise again.

The rising trend is not due to estimator failure, but rather its success in detecting inconsistency between the model and reality. The electric field used in this test case varies smoothly over space, but the estimator assumes it is constant within each region. As more sensors are added, especially within the same region, they begin to diverge in their inferred field values, exposing the limitations of the assumed regional uniformity.

None of the configurations tested yield a cost below the statistical threshold. This is not surprising; the tested estimator's assumptions are deliberately simplified. The cost function reflects both measurement noise and model misfit, and the mismatch between the discrete assumption and the continuous truth introduces unavoidable residuals.

In a real-time environment, the primary output of interest is the estimated electric field, which can inform system awareness and mitigation decisions during a geomagnetic disturbance. While the estimation cost provides insight into how well the assumed model fits the available data, it is not intended as a real-time decision metric. In many cases, measurement coverage may be sparse and fixed, and regions may not perfectly align with field behavior. Even under these constraints, the estimator provides a usable, physically consistent electric field estimation. The cost metric serves as a post-estimation diagnostic, helping operators or planners understand model limitations and assess whether refinement of assumptions or measurement infrastructure may be beneficial over time.

Despite the simplified regional assumptions, the estimator remains capable of producing coherent field estimates that match the overall structure of the true electric field. Its flexibility to scale up, operate with partial data, and provide meaningful diagnostic feedback makes it suitable for real-time deployment on large-scale networks during geomagnetic disturbances.

C. Estimator as a Tool for Assumption Validation

In addition to providing real-time electric field estimates, the estimator supports evaluation of modeling assumptions. The WLS cost function serves as a statistical measure of consistency between the assumed electric field structure and observed GIC and magnetometer data. Higher cost values indicate potential structural mismatch between the model and the true field behavior, particularly when the measurements are redundant or spatial variation is significant.

The estimator accommodates any linear field representation. Assumptions such as uniform fields, regionally discretized fields, or directional constraints can be encoded through the state vector and sensitivity matrices. Because the formulation remains linear, alternate structures can be implemented without the need to modify the estimation algorithm.

This capacity enables structured comparison of different modeling approaches under varying measurement conditions. It provides a quantitative means of identifying when simplifying assumptions are sufficient and when additional spatial flexibility may be necessary to explain observed behavior.

VI. Conclusion and Future Works

Geomagnetic disturbances (GMDs) pose a serious risk to power system stability by inducing low frequency currents, geomagnetically induced currents (GICs), that generate quasi DC voltage drops across transformer windings. These voltages can cause half cycle saturation of transformer cores, increasing magnetizing current, reactive power demand, and producing harmonics that can lead to equipment misoperation and voltage instability. Accurate visualization and evaluation of electric field assumptions is critical for assessing the impact of space weather events.

This paper presents a flexible, measurement driven state estimation algorithm for determining regional electric fields during geomagnetic disturbances. The estimator operates on a linear formulation that maps electric field states to GIC and magnetometer observations. Given a set of regional discretizations and measurement inputs, the method computes a best-fit electric field while providing statistical feedback on how well the assumed model structure aligns with observed data.

Two test systems were used to explore estimator performance. In the 6-bus case, which serves as a conceptual platform, the estimator successfully distinguished between field structures of varying complexity. Estimation cost increased in scenarios where the true field exhibited spatial variation. This variation could not be fully captured by the model's two state representation, which illustrates how cost reflects structural mismatch. These tests also demonstrated that additional measurements only improve performance when the assumed model is capable of representing the variation those measurements reveal.

The 2000-bus synthetic Texas system tested the estimator's scalability under a smoothly varying electric field. Although estimation cost remained above the statistical threshold across all configurations (as expected due to the simplified regional assumptions), the estimator remained stable and informative. The lowest cost occurred when the number of GIC measurements approached three times the number of states, after which the addition of sensors revealed intra-regional variation that was not captured by the piecewise constant model. Despite this structural mismatch, the estimator consistently produced coherent field determinations.

The primary function of the estimator is to generate electric field estimates under practical measurement constraints. It produces spatially coherent results that reflect the best fit to available GIC and magnetometer data. In real-time settings, measurements may be limited, and region layouts fixed. Even in such cases, the estimator provides meaningful results, capturing the best fit electric field consistent with available data. The cost metric complements this capability by indicating when spatial assumptions may warrant refinement.

Several promising directions remain for future research. Sensor placement strategies could be improved to better capture spatial diversity. This method can also be expanded to accommodate larger systems with tens of thousands of buses. Further integration of magnetometer accuracy and resolution into the region definition process would allow for more targeted field modeling. Including evaluation of reactive power losses could expand visibility analysis and potentially help long term transmission system planning. Finally, incorporating nonlinear effects such as harmonic generation during transformer saturation would expand the estimator's capabilities for real time system analysis during geomagnetic events.

Acknowledgments

This material is based upon work supported by the U.S. Department of Energy's Office of Cybersecurity, Energy Security, and Emergency Response (CESER) through project DE-AC05-76RL01830, through a sub-award from Pacific Northwest National Lab (PNNL). The views expressed herein do not necessarily represent the views of the U.S. Department of Energy or the United States Government.

References

[1] J. G. Kappenman, "Storm sudden commencement events and the associated geomagnetically induced current risks to ground-based systems at low-latitude and midlatitude locations," *Space weather*, vol. 1, no. 3, 2003.

[2] D. H. Boteler, "A 21st century view of the march 1989 magnetic storm," *Space weather*, vol. 17, no. 10, pp. 1427–1441, 2019.

[3] V. Albertson, B. Bozoki, W. Feero, J. Kappenman, E. Larsen, D. Nordell, J. Ponder, F. Prabhakara, K. Thompson, and R. Walling, "Geomagnetic disturbance effects on power systems," *IEEE transactions on power delivery*, vol. 8, no. 3, pp. 1206–1216, 1993.

[4] A. Pulkkinen, E. Bernabeu, A. Thomson, A. Viljanen, R. Pirjola, D. Boteler, J. Eichner, P. Cilliers, D. Welling, N. Savani *et al.*, "Geomagnetically induced currents: Science, engineering, and applications readiness," *Space weather*, vol. 15, no. 7, pp. 828–856, 2017.

[5] North American Electric Reliability Corporation, "Effects of geomagnetic disturbances on the bulk power system," 2012.

[6] T. S. Molinski, "Why utilities respect geomagnetically induced currents," *Journal of atmospheric and solar-terrestrial physics*, vol. 64, no. 16, pp. 1765–1778, 2002.

[7] L. Bolduc, "Gic observations and studies in the hydro-québec power system," *Journal of atmospheric and solar-terrestrial physics*, vol. 64, no. 16, pp. 1793–1802, 2002.

[8] L. Rosenqvist, T. Fristedt, A. P. Dimmock, P. Davidsson, R. Fridström, J. Hall, L. Hesslow, J. Kjäll, M. Y. Smirnov, D. Welling *et al.*, "3d modeling of geomagnetically induced currents in sweden—validation and extreme event analysis," *Space Weather*, vol. 20, no. 3, p. e2021SW002988, 2022.

[9] R. Kataoka and C. Ngwira, "Extreme geomagnetically induced currents," *Progress in Earth and Planetary Science*, vol. 3, no. 1, p. 23, 2016.

[10] R. Lesher, J. Porter, and R. Byerly, "Sunburst-a network of gic monitoring systems," *IEEE Transactions on Power Delivery*, vol. 9, no. 1, pp. 128–137, 1994.

[11] D. H. Mac Manus, C. J. Rodger, M. Dalzell, A. W. P. Thomson, M. A. Clilverd, T. Petersen, M. M. Wolf, N. R. Thomson, and T. Divett, "Long-term geomagnetically induced current observations in new zealand: Earth return corrections and geomagnetic field driver," *Space Weather*, vol. 15, no. 8, pp. 1020–1038, 2017. [Online]. Available: https://agupubs.onlinelibrary.wiley.com/doi/abs/10.1002/2017SW001635

[12] C. M. Ngwira, R. Arritt, C. Perry, J. M. Weygand, and R. Sharma, "Occurrence of large geomagnetically induced currents within the epri sunburst monitoring network," *Space Weather*, vol. 21, no. 12, p. e2023SW003532, 2023, e2023SW003532 2023SW003532. [Online]. Available: https://agupubs.onlinelibrary.wiley.com/doi/abs/10.1029/2023SW003532

[13] L. Marti, J. Berge, and R. K. Varma, "Determination of geomagnetically induced current flow in a transformer from reactive power absorption," *IEEE Transactions on Power Delivery*, vol. 28, no. 3, pp. 1280–1288, 2013.

[14] S. Zhang, L.-G. Liu, and H. Li, "Gic influence on uhv power grids based on kalman filter and wams data," *IEEE Access*, vol. 8, pp. 202 379–202 386, 2020.

[15] R. Weigel, "A comparison of methods for estimating the geoelectric field," *Space Weather*, vol. 15, no. 2, pp. 430–440, 2017.

[16] A. Kelbert, C. C. Balch, A. Pulkkinen, G. D. Egbert, J. J. Love, E. J. Rigler, and I. Fujii, "Methodology for time-domain estimation of storm time geoelectric fields using the 3-d magnetotelluric response tensors," *Space Weather*, vol. 15, no. 7, pp. 874–894, 2017.

[17] D. Cordell, M. J. Unsworth, B. Lee, C. Hanneson, D. K. Milling, and I. R. Mann, "Estimating the geoelectric field and electric power transmission line voltage during a geomagnetic storm in alberta, canada using measured magnetotelluric impedance data: The influence of three-dimensional electrical structures in the lithosphere," *Space weather*, vol. 19, no. 10, p. e2021SW002803, 2021.

[18] J. Malone-Leigh, J. Campanyà, P. T. Gallagher, M. Neukirch, C. Hogg, and J. Hodgson, "Nowcasting geoelectric fields in ireland using magnetotelluric transfer functions," *Journal of Space Weather and Space Climate*, vol. 13, p. 6, 2023.

[19] G. P. Juvekar, C. Klauber, K. R. Davis, T. J. Overbye, and K. Shetye, "Gic-inclusive state estimator for power system awareness during geomagnetic disturbance events," *IEEE Transactions on Power Systems*, vol. 36, no. 4, pp. 2966–2974, 2020.

[20] J. Xie, A. S. Meliopoulos, B. Xie, C. Zhong, and K. Liu, "Geoelectric field estimation during geomagnetic disturbances," in *2019 IEEE Power & Energy Society General Meeting (PESGM)*. IEEE, 2019, pp. 1–5.

[21] M. Clilverd, C. Rodger, D. H. M. Manus, J. Brundell, M. Dalzell, A. Renton, V. Lo, A. Lapthorn, A. Smith, J. Malone-Leigh *et al.*, "Geomagnetically induced currents, transformer harmonics, and reactive power impacts of the gannon storm in may 2024," *Space Weather*, vol. 23, no. 4, p. e2024SW004235, 2025.

[22] North American Electric Reliability Corporation (NERC), "TPL-007-4 – Transmission System Planned Performance for Geomagnetic Disturbance Events," https://www.nerc.com/pa/Stand/Project2023TPL0074/Pages/default.aspx, 2023, NERC Standard.

[23] F. E. R. Commission *et al.*, "Reliability standard for transmission system planned performance for geomagnetic disturbance events," Technical Report, Tech. Rep., 2015.

[24] A. Monticelli, *State Estimation in Electric Power Systems: A Generalized Approach*. Springer, 1999.

[25] A. Abur and A. G. Exposito, *Power system state estimation: theory and implementation*. CRC press, 2004.

[26] E. Kalnay, M. Kanamitsu, R. Kistler, W. Collins, D. Deaven, L. Gandin, M. Iredell, S. Saha, G. White, J. Woollen *et al.*, "The ncep/ncar 40-year reanalysis project," in *Renewable energy*. Routledge, 2018, pp. Vol1_146–Vol1_194.

[27] R. Pirjola, "Review on the calculation of surface electric and magnetic fields and geomagnetically induced currents (gics) in ground-based technological systems," *Surveys in Geophysics*, vol. 23, no. 1, pp. 71–90, 2002.

[28] I. Erinmez, J. G. Kappenman, and W. A. Radasky, "Management of the geomagnetically induced current risks on the national grid company's electric power transmission system," *Journal of Atmospheric and Solar-Terrestrial Physics*, vol. 64, no. 5, pp. 743–756, 2002, space Storms and Space Weather. [Online]. Available: https://www.sciencedirect.com/science/article/pii/S1364682602000366

[29] L. Marti, A. Rezaei-Zare, and D. Boteler, "Calculation of induced electric field during a geomagnetic storm using recursive convolution," *IEEE Transactions on Power Delivery*, vol. 29, no. 2, pp. 802–807, 2014.

[30] V. D. Albertson and J. A. Van Baelen, "Electric and magnetic fields at the earth's surface due to auroral currents," *IEEE Transactions on Power Apparatus and Systems*, no. 4, pp. 578–584, 1970.

[31] P. Fernberg, "One-dimensional earth resistivity models for selected areas of continental united states and alaska," *EPRI technical update*, vol. 1026430, pp. 1–190, 2012.

[32] A. Kelbert, P. A. Bedrosian, and B. S. Murphy, "The first 3d conductivity model of the contiguous united states: Reflections on geologic structure and application to induction hazards," *Geomagnetically induced currents from the Sun to the power grid*, pp. 127–151, 2019.

[33] D. Boteler and R. Pirjola, "Comparison of methods for modelling geomagnetically induced currents," in *Annales Geophysicae*, vol. 32, no. 9. Copernicus Publications Göttingen, Germany, 2014, pp. 1177–1187.

[34] T. J. Overbye, T. R. Hutchins, K. Shetye, J. Weber, and S. Dahman, "Integration of geomagnetic disturbance modeling into the power flow: A methodology for large-scale system studies," in *2012 north american power symposium (naps)*. IEEE, 2012, pp. 1–7.

[35] M. Kazerooni, H. Zhu, T. J. Overbye, and D. A. Wojtczak, "Transmission system geomagnetically induced current model validation," *IEEE Transactions on Power Systems*, vol. 32, no. 3, pp. 2183–2192, 2016.

[36] U. Bui, T. J. Overbye, K. Shetye, H. Zhu, and J. Weber, "Geomagnetically induced current sensitivity to assumed substation grounding resistance," in *2013 North American Power Symposium (NAPS)*. IEEE, 2013, pp. 1–6.

[37] R. Horton, D. Boteler, T. J. Overbye, R. Pirjola, and R. C. Dugan, "A test case for the calculation of geomagnetically induced currents," *IEEE Transactions on Power Delivery*, vol. 27, no. 4, pp. 2368–2373, 2012.

[38] V. Albertson, J. Thorson, and S. Miske, "The effects of geomagnetic storms on electrical power systems," *IEEE Transactions on Power Apparatus and Systems*, no. 4, pp. 1031–1044, 1973.

[39] S. Saleh, E. W. Zundel, G. Young-Morris, D. Jewett, S. Brown, E. F. Hill, and J. Meng, "Investigating harmonic distortion in power transformers due to geomagnetically induced current flows," *IEEE Transactions on Industry Applications*, vol. 59, no. 5, pp. 5432–5442, 2023.

[40] "High-impact, low-frequency event risk to the north american bulk power system," *North American Electric Reliability Corporation (NERC)*, 2010.

[41] A. Pulkkinen, S. Lindahl, A. Viljanen, and R. Pirjola, "Geomagnetic storm of 29–31 october 2003: Geomagnetically induced currents and their relation to problems in the swedish high-voltage power transmission system," *Space weather*, vol. 3, no. 8, 2005.

[42] N. C. LoGiudice, J. M. Snodgrass, and T. J. Overbye, "Estimating the electric field from geomagnetically induced currents," in *2024 IEEE Kansas Power and Energy Conference (KPEC)*, 2024, pp. 1–4.

[43] A. B. Birchfield, T. Xu, K. M. Gegner, K. S. Shetye, and T. J. Overbye, "Grid structural characteristics as validation criteria for synthetic networks," *IEEE Transactions on power systems*, vol. 32, no. 4, pp. 3258–3265, 2016.

[44] L. Lowery and A. B. Birchfield, "Voltage stability interface limits in non-uniform geomagnetic disturbances," in *2024 56th North American Power Symposium (NAPS)*. IEEE, 2024, pp. 1–6.

[45] B. McFee, "kmeans-constrained: Constrained kmeans clustering for python," https://github.com/bmcfee/kmeans-constrained, 2020, accessed: 2025-05-17.

[46] C. Klauber, K. S. Shetye, Z. Mao, T. J. Overbye, J. Gannon, and M. Henderson, "Real-time monitoring applications for the power grid under geomagnetic disturbances," in *2020 IEEE Electric Power and Energy Conference (EPEC)*. IEEE, 2020, pp. 1–5.

[47] K. S. Shetye, R. R. Kumar, C. Klauber, Z. Mao, T. J. Overbye, J. Gannon, and M. Henderson, "Development and electric grid applications of a magnetometer network," *IEEE Open Access Journal of Power and Energy*, vol. 8, pp. 77–84, 2021.